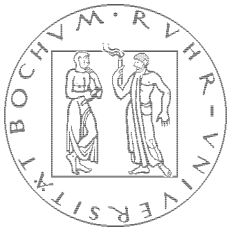

Preprint 01-2003

3D modeling of strong discontinuities in elastoplastic solids: Fixed and rotating localization formulations

J. Mosler and G. Meschke

Ruhr University Bochum

This is a preprint of an article published in:

International Journal for Numerical Methods in Engineering, Vol. 57, 1553–1576, (2003)

3D modeling of strong discontinuities in elastoplastic solids: Fixed and rotating localization formulations

J. Mosler

Lehrstuhl für Technische Mechanik
Ruhr University Bochum
Universitätsstr. 150,D-44780 Bochum, Germany
E-Mail: mosler@tm.bi.ruhr-uni-bochum.de
URL: www.tm.bi.ruhr-uni-bochum.de/mosler

G. Meschke

Institute for Structural Mechanics
Ruhr University Bochum
Universitätsstr. 150, D-44780 Bochum, Germany
E-Mail: guenther.meschke@sd.ruhr-uni-bochum.de
URL: www.sd.ruhr-uni-bochum.de

SUMMARY

This paper is concerned with the incorporation of displacement discontinuities into a continuum theory of elastoplasticity for the modeling of localization processes such as cracking in brittle materials. Based on the Strong Discontinuity Approach (SDA) [1] mesh objective 2D and 3D finite element formulations are developed using linear and quadratic 2D elements as well as 8-noded 3D elements. In the formulation of the finite element model proposed in the paper, the analogy with standard formulations is emphasized. The parameter defining the amplitude of the displacement jump within the finite element is condensed out at the material level without employing the standard static condensation technique. This approach results in linearized constitutive equations formally identical to continuum models. Therefore the standard return mapping algorithm is used to solve the nonlinear equations. In analogy to concepts used in continuum smeared crack models, a rotating formulation of the SDA is proposed in addition to the standard concept of fixed discontinuities. It is shown, that the rotating localization approach reduces locking effects observed in analyses based on fixed localization directions. The applicability of the proposed SDA finite element model as well as its numerical performance is investigated by means of a three-dimensional ultimate load analysis of a steel anchor embedded in a concrete block subjected to a shear force.

1 INTRODUCTION

Numerical analyses of structures loaded up to and beyond ultimate load require adequate models for the description of failure and of the post-failure behavior of the material. In many materials, in particular in quasi-brittle materials, material failure is characterized by a strongly discontinuous failure mode associated with jumps in the displacement field across the failure zone. Typical examples are cracks in cement-based materials or shear failure in overconsolidated soils.

The mathematical and numerical implications of strain localization such as loss of ellipticity and lack of invariance with respect to the spatial discretization and the need for enhanced continuum models to overcome these problems have been extensively addressed in the recent decade, see, e.g. [2] for an overview and references therein. By now established techniques for the analysis of strain localization problems in a continuum mechanics framework, such as nonlocal models [3, 4], gradient-enhanced models [5, 6] and COSSERAT continua [7, 8] make use of an internal length parameter related to the specific material. This approach, however, requires a sufficiently fine resolution of the localization zone to guarantee mesh objectivity. In

large scale structural computations the required computational costs may be prohibitive even if adaptive techniques are used.

As an alternative method, the so-called Strong Discontinuity Approach (SDA) has been proposed by SIMO, OLIVER & ARMERO [1]. In this concept, the localization zone is represented as a surface of discontinuous displacements within the respective finite elements. This method accounts for the multi-scale character of the problem (the failure zone is several dimensions smaller than the structure) and allows to use relatively large elements compared to the width of the localization zone. Hence, this method is suitable for large scale structural applications.

More recently, the concept of discontinuous displacements has been incorporated within a finite element formulation based on the Partition of Unity concept [9]. In this approach, the displacement discontinuities are represented by means of additional degrees of freedom [10]. Although this promising approach opens perspectives for a completely mesh-independent modeling of failure zones such as cracks, considerable complexities are involved in particular in 3D implementations of the method, considering multiple or crossing failure surfaces, which do not seem to be fully resolved so far.

In the SDA, displacement jumps are embedded locally in the respective finite elements without affecting neighboring elements. In accordance with the underlying enhanced assumed strain (EAS) concept, only the (enhanced) strains resulting from the discontinuous displacement field appear explicitely in the formulation. The idea to enhance standard finite element models by additional modes to capture displacement jumps has been already suggested in the early work by JOHNSON & SCOTT [11]. Since then, several variants of this concept have been proposed [12–14]. A more detailed insight into the incorporation of strong displacement discontinuities into classical (local) elastoplastic and elasto-damage continuum models was provided by SIMO, OLIVER & ARMERO [1]. This formulation corresponds to a PETROV-GALERKIN method in the sense that the weak form involves test functions different from the variations of the enhanced strains. With the exception of [15, 16], the existing implementations of the SDA are based on triangular [17–20] and tetrahedral [21] elements, respectively. In these references the localization zones are assumed to have a fixed orientation after the onset of failure. Hence these approaches correspond to the class of fixed crack models frequently used in the past in the context of smeared crack analyses of concrete structures (see e.g. [22, 23]).

In this paper, a 3D formulation of the SDA for failure analyses of elastoplastic materials using bi- and tri-linear displacement interpolations in 2D quadrilateral and 3D cubic elements is proposed. Several extensions and modifications are incorporated. As an alternative to the assumption of a fixed localization surface followed in previous formulations, a dependence of the localization surface on the deformation in analogy to plasticity-based smeared crack models (e.g. [24, 25] is taken into account in the proposed model. Allowing for rotations of the localization zone (such as cracks) reduces the effect of stress locking [26] previously reported in [19] and also demonstrated in the paper by means of a comparison between a rotating and a fixed crack formulation. As far as the interface law along the surface of discontinuity is concerned, a continuum approach is followed in the sense that the traction separation law is obtained from the projection of an elastoplastic continuum model onto the localization surface.

The proposed formulation results in a computational algorithm, which is formally identical to standard non-associative plasticity models, requiring only minor modifications of standard plasticity models. In contrast to the static condensation of the parameter defining the amplitude of the displacement jump [1, 19, 27], this parameter is determined at the material level, using the standard return-mapping algorithm. The enhanced strains are added only at the integration-point level, leaving the element routines unaffected.

The bulk of the published implementations of the SDA is concerned with triangular finite elements [17, 19, 27]. In this case, the constant stress field within the element results in a simple

condition for the onset of localization. The behavior of the considered finite element is either purely elastic, or only one enhanced strain field has to be added to the standard GALERKIN strains, since a straight localization line always separates one from two other nodes. An extension of the SDA model to bi-linear (tri-linear) quadrilateral (brick) elements requires the consideration of one (three) additional configurations of possible localization surfaces [28]. In the paper, implementations of the proposed formulation of the SDA within 4-node bilinear and 8-node tri-linear elements are investigated. Algorithmic issues and details of the implementation of both rotating and fixed crack formulations are addressed.

The paper is organized as follows: Sections 2 and 3 are concerned with a concise review of the basic kinematic assumptions of the SDA within a geometrically linear setting and with the re-formulation of a standard model of plasticity within the concept of strong discontinuities. The design of discontinuous displacement fields in 2D and 3D elements using a fixed and a rotating localization approach as well as the numerical integration by means of the return mapping algorithm are addressed in Section 4. Subsection 4.2 is concerned with a rotating crack formulation while the respective formulation for a fixed crack approach is given in Subsection 4.3. These considerations are not restricted to a particular plasticity model. The numerical application in Section 5 is concerned with the three-dimensional re-analysis of a shear test of a steel anchor embedded within a concrete block by means of an 8-node SDA-based finite element. In these analyses only mode I failure is taken into account.

2 KINEMATICS: DISCONTINUITIES IN THE DISPLACEMENT FIELD

This section contains a concise review of the Strong Discontinuity Approach (SDA) as proposed in [1, 29–31] and further elaborated in [15, 18, 20, 27, 32–34].

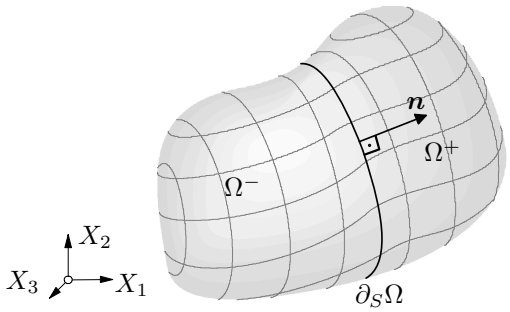

Figure 1: Body $\mathcal{B}$ separated by a localization surface $\partial_{\mathrm{s}}\Omega$ into two parts Ω^- and Ω^+

A domain Ω of a body $\mathcal{B}$ is considered to be separated into two portions Ω^- and Ω^+ by means of a localization surface $\partial_{\mathrm{s}}\Omega$ (Figure 1). This surface is defined by its normal $\boldsymbol{n}$. Based on the assumption of a jump in the displacement field across this surface, an additive decomposition of the displacement field

$$\boldsymbol{u}(\boldsymbol{x}) = \bar{\boldsymbol{u}}(\boldsymbol{x}) + \hat{\boldsymbol{u}}(\boldsymbol{x}), \qquad \forall\, \boldsymbol{x} \in \Omega, \quad \text{with:} \quad \hat{\boldsymbol{u}}(\boldsymbol{x}) = [\![\boldsymbol{u}]\!]\; M_{\mathrm{s}}(\boldsymbol{x}) \tag{1}$$

into a regular part $\bar{\boldsymbol{u}}(\boldsymbol{x})$ and a jump term $\hat{\boldsymbol{u}}(\boldsymbol{x})$ (see Figure 2) is assumed [1, 29–31].

The function $M_{\mathrm{s}}(\boldsymbol{x})$ can be decomposed into a HEAVISIDE function $H_{\mathrm{s}}(\boldsymbol{x})$ and a smooth function $\varphi(\boldsymbol{x})$

$$M_{\mathrm{s}}(\boldsymbol{x}) = H_{\mathrm{s}}(\boldsymbol{x}) - \varphi(\boldsymbol{x}), \qquad \forall\, \boldsymbol{x} \in \Omega. \tag{2}$$

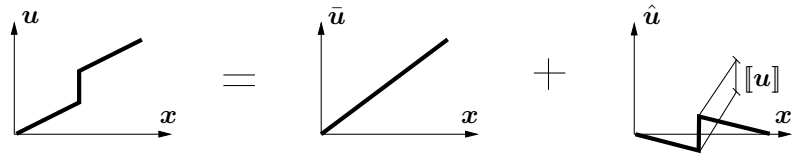

Figure 2: Additive decomposition of the displacement field into a regular part $\bar{\boldsymbol{u}}$ and a part $\hat{\boldsymbol{u}}$ which contains a jump

The function $\varphi(\boldsymbol{x})$ allows to prescribe the boundary conditions in terms of $\bar{\boldsymbol{u}}$. At the localization surface

$$[\![M_{\mathrm{s}}(\boldsymbol{x})]\!] = 1, \qquad \forall\, \boldsymbol{x} \;\in\; \partial_{\mathrm{s}}\Omega \tag{3}$$

has to be fulfilled. From computing the gradient of Equation (1), using Equation (2), together with the derivative of the HEAVISIDE function $\boldsymbol{\nabla} H_{\mathrm{s}} = \boldsymbol{n}\delta_{\mathrm{s}}$ [35], the linearized strain tensor is obtained as (see e.g. [17] for more details)

$$\boldsymbol{\varepsilon}(\boldsymbol{u}) = \boldsymbol{\nabla}^{\mathrm{sym}}\boldsymbol{u} = \boldsymbol{\nabla}^{\mathrm{sym}}\bar{\boldsymbol{u}} - \underbrace{([\![\boldsymbol{u}]\!] \otimes \boldsymbol{\nabla}\varphi)^{\mathrm{sym}}}_{\tilde{\boldsymbol{\varepsilon}}} + \underbrace{([\![\boldsymbol{u}]\!] \otimes \boldsymbol{n})^{\mathrm{sym}}}_{\boldsymbol{\varepsilon}_\delta}\; \delta_{\mathrm{s}}. \tag{4}$$

δ_{s} denotes the DIRAC-delta distribution. In Equation (4) it has been assumed, that $\boldsymbol{\nabla}\,[\![\boldsymbol{u}]\!] = \boldsymbol{0}$. This assumption is motivated by the finite element implementation of the model, which is characterized by a constant direction and amplitude of the displacement jump with respect to the spatial coordinates within the domain Ω. The modified strain tensor (4) contains, in addition to the gradient of the smooth part of the displacement field, two additional parts, a regular part $\tilde{\boldsymbol{\varepsilon}} \in \Omega$ and the singular distribution $\boldsymbol{\varepsilon}_\delta \in \partial_{\mathrm{s}}\Omega$. To simplify the following derivations, the rate of the displacement jump is represented by

$$[\![\dot{\boldsymbol{u}}]\!] = \dot{\zeta}\, \boldsymbol{m}, \tag{5}$$

with the vector $\boldsymbol{m}$ defining the direction of the jump, and the rate of the amplitude of the jump ζ. The vectors $\boldsymbol{n}$ and $\boldsymbol{m}$ are computed from a bifurcation analysis, characterized by the localization condition

$$\boldsymbol{Q}^{\mathrm{perf}} \cdot \boldsymbol{m} = \boldsymbol{0}, \tag{6}$$

with the acoustic tensor $\boldsymbol{Q}^{\mathrm{perf}}$ defined as (see [1, 36])

$$\boldsymbol{Q}^{\mathrm{perf}} = \boldsymbol{n} \cdot \mathbb{C}_T^{\mathrm{perf}} \cdot \boldsymbol{n}. \tag{7}$$

$\mathbb{C}_T^{\mathrm{perf}}$ is the perfect plastic tangent operator.

3 PLASTICITY THEORY FORMULATED WITHIN THE STRONG DISCONTINUITY APPROACH

In this section, the concept of strong discontinuities is incorporated within the governing equations of classical non-associated plasticity theory. It follows to a large extent previous formulations, as e.g. [1, 17, 27]. After the re-formulation of the flow-rule and the plastic multiplier in the context of the SDA a model for mode-I failure based upon the principal stress criterion is taken as a particular example.

Without referring to any particular model of plasticity for now, the space of admissible stresses

$$\mathbb{E}_{\boldsymbol{\sigma}} := \{(\boldsymbol{\sigma}, \boldsymbol{q}) \in \mathbb{S} \times \mathrm{R}^n \mid \phi(\boldsymbol{\sigma}, \boldsymbol{q}) \leq 0\}\,, \tag{8}$$

with $\mathbb{S}$ defining the group of symmetric rank two tensors, is defined by means of a yield (failure) function $\phi(\boldsymbol{\sigma}, \boldsymbol{q})$, which depends on the stress tensor and a vector of stress-like hardening/softening parameters $\boldsymbol{q}$. The model is constituted by the definition of the stress rate, the evolution of the plastic strains and the internal variables $\hat{\boldsymbol{\alpha}}$ conjugate to $\boldsymbol{q}$ in the form

$$\begin{aligned} \dot{\boldsymbol{\sigma}} &= \mathbb{C} : (\dot{\boldsymbol{\varepsilon}} - \dot{\boldsymbol{\varepsilon}}^{\mathrm{p}})\,, \\ \dot{\boldsymbol{\varepsilon}}^{\mathrm{p}} &= \lambda\, \frac{\partial g(\boldsymbol{\sigma}, \boldsymbol{q})}{\partial \boldsymbol{\sigma}}, \\ \dot{\hat{\boldsymbol{\alpha}}} &= \lambda\, \frac{\partial h(\boldsymbol{\sigma}, \boldsymbol{q})}{\partial \boldsymbol{q}}. \end{aligned} \tag{9}$$

$\mathbb{C}$ is the elastic 4th order constitutive tensor assumed as constant, $g(\boldsymbol{\sigma}, \boldsymbol{q})$ and $h(\boldsymbol{\sigma}, \boldsymbol{q})$ are potential functions and λ is the plastic multiplier. The model is completed by the KUHN-TUCKER conditions $\lambda \geq 0$, $\phi \leq 0$, $\lambda\, \phi = 0$. From the regular distribution of the stress tensor follows that the plastic multiplier λ,

$$\lambda = \bar{\lambda} + \lambda_\delta \delta_{\mathrm{s}}, \tag{10}$$

must consist of a singular part $\lambda_\delta \delta_{\mathrm{s}}$ in addition to a regular part $\bar{\lambda}$ [1]. In what follows, it is assumed that $\bar{\lambda} = 0$. Consequently, as a localization surface develops, plastic deformations are restricted to the surface of discontinuity $\partial_{\mathrm{s}}\Omega$, while in the remaining part of the considered domain

$$\dot{\boldsymbol{\varepsilon}}^{\mathrm{p}} = \boldsymbol{0}, \quad \forall\, \boldsymbol{x} \in \Omega^-, \Omega^+. \tag{11}$$

From Equations (4), (9) and (10) together with (11) and from the traction continuity requirement follows, that the plastic strains $\boldsymbol{\varepsilon}^{\mathrm{p}}$ are related to the assumed singular strains

$$\dot{\boldsymbol{\varepsilon}}^{\mathrm{p}} = (\llbracket \dot{\boldsymbol{u}} \rrbracket \otimes \boldsymbol{n})^{\mathrm{sym}}\ \delta_{\mathrm{s}} = \lambda_\delta\, \frac{\partial g(\boldsymbol{\sigma}, \boldsymbol{q})}{\partial \boldsymbol{\sigma}}\ \delta_{\mathrm{s}}. \tag{12}$$

Using the consistency condition $\dot{\phi} = 0$, the singular plastic multiplier λ_δ can be computed by means of the amplitude of the displacement jump ζ as

$$\lambda_\delta = \dot{\zeta} \frac{\partial_{\boldsymbol{\sigma}} \phi : \mathbb{C} : (\boldsymbol{m} \otimes \boldsymbol{n})^{\mathrm{sym}}}{\partial_{\boldsymbol{\sigma}} \phi : \mathbb{C} : \partial_{\boldsymbol{\sigma}} g}. \tag{13}$$

For details concerning the assumptions leading to Equation (13) see, e.g. [17].

In what follows, the simple case of positively homogeneous yield functions of degree one, e.g.

$$\phi(\boldsymbol{\sigma}, \hat{\alpha}) = (\boldsymbol{m} \otimes \boldsymbol{n}) : \boldsymbol{\sigma} - q(\hat{\alpha}), \tag{14}$$

together with an associative flow model will be used. Inserting Equation (14) into Equation (13) and assuming the postulate of maximum dissipation, which implies that $g(\boldsymbol{\sigma}, q) = \phi(\boldsymbol{\sigma}, q)$ and $h(\boldsymbol{\sigma}, q) = -\phi(\boldsymbol{\sigma}, q)$, leads to

$$\lambda_\delta = \dot{\zeta}. \tag{15}$$

From the evolution equation $(9)_3$ for the strain-like internal variable $\hat{\alpha}$ we obtain

$$\dot{\hat{\alpha}} = \lambda_\delta\ \delta_{\mathrm{s}} = \frac{\partial \hat{\alpha}}{\partial q}\ \dot{q} =: \hat{H}^{-1}\ \dot{q}. \tag{16}$$

Since the stress-like variable q represents a regular distribution, the plastic modulus $\hat{H}$ has to be interpreted as a singular distribution (see e.g. [1]) resulting in

$$\hat{H}^{-1} = H^{-1}\,\delta_{\mathrm{s}} \quad \Rightarrow \quad \lambda_\delta = \dot{\zeta} = H^{-1}\,\dot{q}. \tag{17}$$

Consequently, Equation (14) can be re-written as

$$\phi(\boldsymbol{\sigma},\alpha) = (\boldsymbol{m}\otimes\boldsymbol{n}) : \boldsymbol{\sigma} - q(\alpha) = 0, \quad \text{with} \quad \dot{\alpha} := |\dot{\zeta}|. \tag{18}$$

In contrast to Equation (14), $\phi(\boldsymbol{\sigma},\alpha) = 0$ with ϕ according to Equation (18) now represents a traction separation law for the component $t_m := (\boldsymbol{m}\otimes\boldsymbol{n}) : \boldsymbol{\sigma}$ of the traction vector.

For the special case $\boldsymbol{m} = \boldsymbol{n}$, the RANKINE failure criterion, suitable for the representation of mode-I failure in brittle materials, is recovered. In this case, $\boldsymbol{n}$ coincides with the direction of the maximum principal stress. The stress component $(\boldsymbol{n}\otimes\boldsymbol{n}) : \boldsymbol{\sigma}$ normal to the fracture surface is controlled by the failure criterion

$$\phi(\boldsymbol{\sigma},\alpha) = (\boldsymbol{n}\otimes\boldsymbol{n}) : \boldsymbol{\sigma} - q(\alpha). \tag{19}$$

In the numerical analyses contained in Subsection 4.4 and Section 5, respectively, this type of failure criterion will be employed.

4 FINITE ELEMENT FORMULATION OF SDA-BASED ELASTOPLASTIC MODELS USING BI- AND TRI-LINEAR FINITE ELEMENTS

This section contains 2D and 3D finite element formulations of elastoplastic models using embedded displacement discontinuities. In contrast to previous formulations of the Strong Discontinuity concept [1, 17, 18, 20, 32], the present implementation of the SDA is restricted to the material point level only [37], circumventing completely the need for static condensation. A similar approach was recently proposed in [38]. Subsection 4.1 contains the design of the enhanced strain fields in bi- and tri-linear as well as in bi-quadratic finite elements. Details of the integration scheme and the linearization of the set of nonlinear equations are given in Subsection 4.2 and 4.3 for a rotating and fixed localization formulation, respectively.

4.1 Design of the enhanced strains

Using Equations (5) and (4), the enhanced strains associated with the discontinuous displacement field within the domain $\Omega^{\pm}$ of the finite element can be defined in rate form by means of a second order tensor $\boldsymbol{G}$ as

$$\dot{\tilde{\boldsymbol{\varepsilon}}} = \boldsymbol{G}\,\dot{\zeta}, \tag{20}$$

with

$$\boldsymbol{G} = (\boldsymbol{\nabla}\varphi\otimes\boldsymbol{m})^{\mathrm{sym}}. \tag{21}$$

ζ denotes the amplitude of the displacement jump. In what follows, the smooth function $\varphi(\boldsymbol{\xi})$ in Equation (21) will be specified. Since this function has to comply with the DIRICHLET boundary conditions, the gradient of φ

$$\boldsymbol{\nabla}\varphi(\boldsymbol{x}) = \sum_{i=1}^{n_{\Omega^+}} \frac{\partial N_i(\boldsymbol{\xi})}{\partial \boldsymbol{x}}, \tag{22}$$

computed by means of the interpolation functions $N_i(\boldsymbol{\xi})$ corresponding to the nodes i in Ω^+ is a suitable choice [39]. Figure 3 shows two possible modes of the function $M_{\mathrm{s}}(\boldsymbol{\xi}) = H_{\mathrm{s}}(\boldsymbol{\xi}) - \varphi(\boldsymbol{\xi})$ for a plane 4-node finite element. Since $M_{\mathrm{s}}(\boldsymbol{\xi})$ can be expressed as a sum of standard interpolation functions, $M_{\mathrm{s}}(\boldsymbol{\xi})$ is bi-linear in $\boldsymbol{\xi}$ for this element type. An extension to bi-quadratic shape

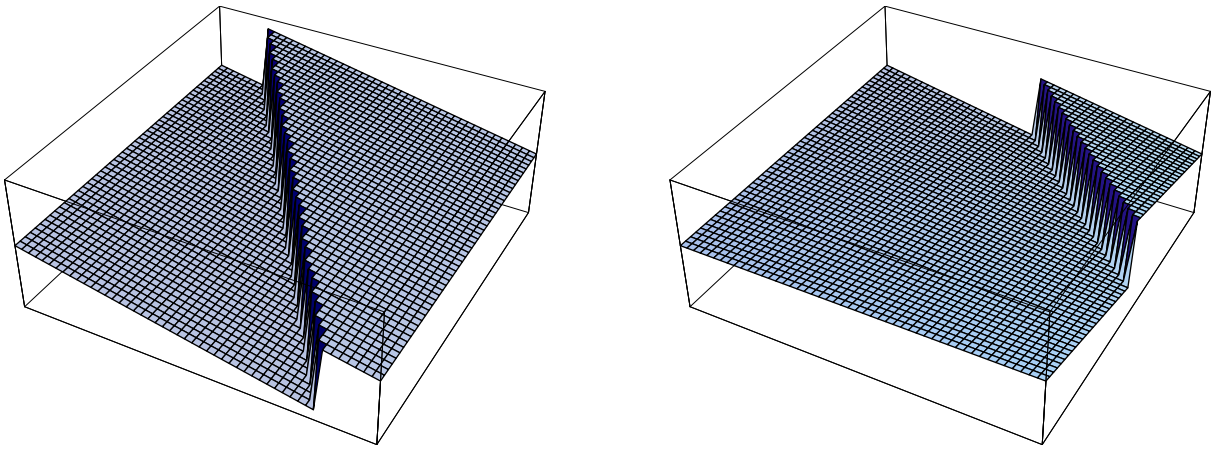

a) b)

Figure 3: Two possible modes of the discontinuous shape function $M_{\mathrm{s}}(\boldsymbol{x})$ using bi-linear functions. a) A localization surface is cutting two opposite edges of the finite element, b) a localization surface is cutting two adjacent edges of the finite element

functions was investigated recently in [40]. The shape of the approximated discontinuous displacements resulting from bi-quadratic shape-functions is shown in Figure 4 for two possible locations of the failure surface. In [28] the SDA-concept was extended to 8-node brick ele-

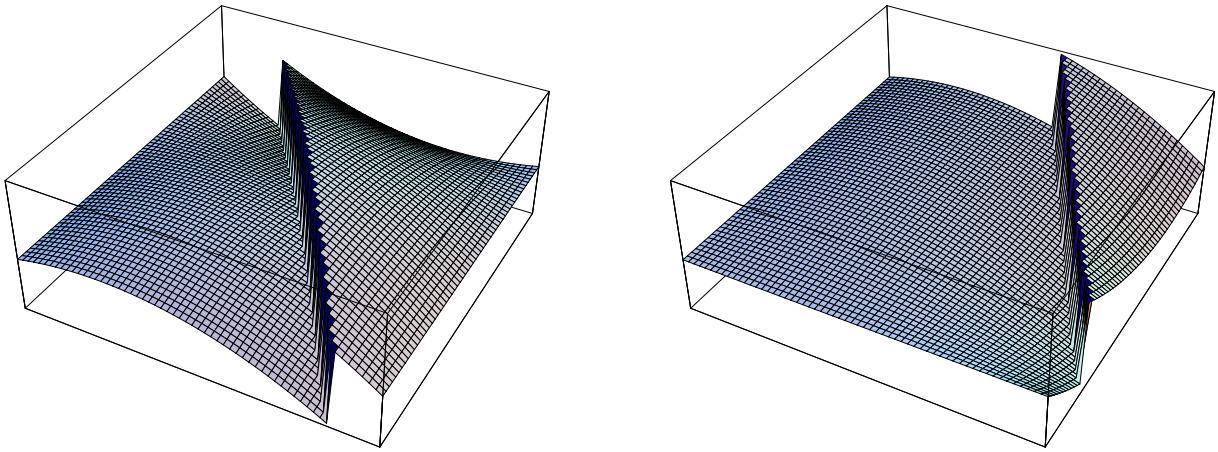

a) b)

Figure 4: Two possible modes of the discontinuous shape function $M_{\mathrm{s}}(\boldsymbol{x})$ using bi-quadratic functions. a) A localization surface is cutting two opposite edges of the finite element, b) a localization surface is cutting two adjacent edges of the finite element

ments with tri-linear interpolation functions. The four different possible configurations of the localization surface within a tri-linear 8-node element are illustrated in Figure 5.

According to standard computational plasticity, the constitutive equations and, more precisely, the yield criterion is enforced in a discrete set of integration points. If material instability

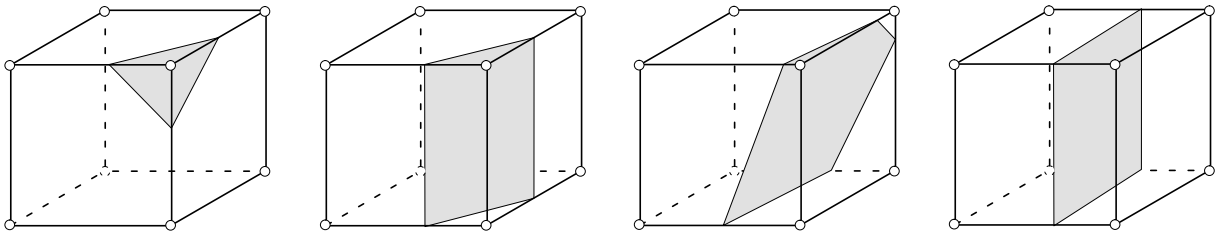

Figure 5: Four possible configurations of the localization surface within an 8-noded brick element: a) A localization surface separates one node, b) a localization surface separates two nodes, c) a localization surface separates three nodes, d) a localization surface separates four nodes

is signalled according to criterion (6), the tensor of enhanced strains (20) is computed in the respective GAUSS points. As the localization criterion is determined in discrete GAUSS points, these points must be part of the localization zone. The orientation $\boldsymbol{n}$ of the discontinuity is determined on the basis of the stress state in this point. In general, the direction of the normal vector $\boldsymbol{n}$ of the failure surface is different in each of the integration points. Figure 6 illustrates a possible, although unrealistic situation with different directions of $\boldsymbol{n}$ in two GAUSS points within a 4-node element. The discontinuous part of the displacement field corresponding to these GAUSS points are shown in Figure 6b and 6c, respectively.

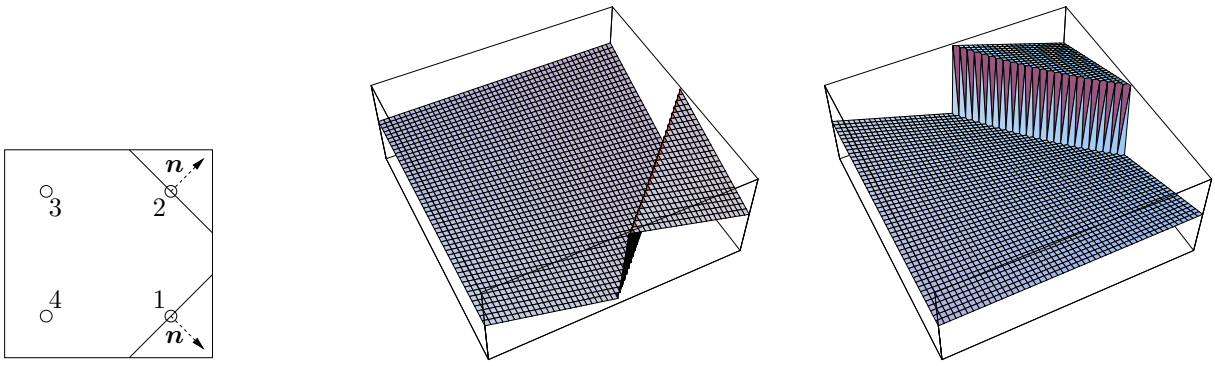

Figure 6: A plane 4-node element with two active localization surfaces: a) Finite element and normal vectors $\boldsymbol{n}$ in the respective GAUSS-points, b) $M_{\mathrm{s}}(\boldsymbol{x})$ associated with GAUSS-point 1, c) $M_{\mathrm{s}}(\boldsymbol{x})$ associated with GAUSS-point 2

The rate of the displacement jump amplitude ζ in Equation (20) can be determined by means of the yield condition

$$\phi(\boldsymbol{\sigma}, \zeta) = (\boldsymbol{m} \otimes \boldsymbol{n}) : \boldsymbol{\sigma} - q(\zeta) = 0 \quad \forall \boldsymbol{x} \in \partial_{\mathrm{s}}\Omega. \tag{23}$$

In the context of the finite element implementation, the solution of Equation (23) is not trivial for general types of finite elements since $\boldsymbol{\sigma}$ depends on $\boldsymbol{G}$ via Equations $(9)_1$ and (20). Hence, as will be shown in the following, the weak form of the traction equilibrium will be used instead of the strong form (23).

The majority of finite element formulations using the strong discontinuity approach is based on two-dimensional triangular [17, 19, 20] and three-dimensional tetrahedral elements [21].

Due to the low order approximation of the displacements, constant interpolations of the strains and stresses follow. Consequently, $\dot{\tilde{\boldsymbol{\varepsilon}}}$ is also constant for each element and only one GAUSS point has to be considered. In this case, $\boldsymbol{G}$ is a constant second order tensor and the behavior of the respective finite element is either purely elastic or purely localized. This simplification, however, does not hold for other types of finite elements. Hence, in general, $\boldsymbol{G}$ depends on the spatial coordinates (see Figure 6).

The failure surface (23) represents a traction separation law of the format

$$t_{m,\mathrm{s}} = q(\zeta), \quad \text{with} \quad t_{m,\mathrm{s}} := (\boldsymbol{m} \otimes \boldsymbol{n}) : \boldsymbol{\sigma}|_{\partial_{\mathrm{s}}\Omega} \tag{24}$$

falling into the more general class of constitutive interface laws characterized by

$$\boldsymbol{t}_{\mathrm{s}} = \boldsymbol{t}_{\mathrm{s}}(\llbracket \boldsymbol{u} \rrbracket), \quad \text{with} \quad \boldsymbol{t}_{\mathrm{s}} = \boldsymbol{n} \cdot \boldsymbol{\sigma}|_{\partial_{\mathrm{s}}\Omega}. \tag{25}$$

In addition to Equation (25), the traction equilibrium

$$\llbracket \boldsymbol{t} \rrbracket = \boldsymbol{t}^{+} - \boldsymbol{t}^{-} = \boldsymbol{0} \tag{26}$$

has to be fulfilled at the localization surface. According to [30], the coupling between the Equations (26) and (25) is provided by the condition $\boldsymbol{t}_{\mathrm{s}} = \boldsymbol{t}^{+}$ leading to

$$\boldsymbol{t}^{+} = \boldsymbol{t}_{\mathrm{s}} \quad \Rightarrow \quad \boldsymbol{t}^{+} = \boldsymbol{t}_{\mathrm{s}}(\llbracket \boldsymbol{u} \rrbracket). \tag{27}$$

This condition follows from the principle of virtual work for continua with an internal surface using discontinuous displacement fields and test functions (see [30]). For the considered failure criterion (23) one obtains

$$t_m^{+} = (\boldsymbol{m} \otimes \boldsymbol{n}) : \boldsymbol{\sigma}^{+} = t_m^{-} = (\boldsymbol{m} \otimes \boldsymbol{n}) : \boldsymbol{\sigma}^{-} = t_{m,\mathrm{s}} = q(\zeta). \tag{28}$$

Since $\boldsymbol{G}$, and consequently $\boldsymbol{\sigma}$, are dependent on the spatial coordinates, the rate of the amplitude of the displacement jump ζ across the localization surface cannot be computed from the local form (28).

In accordance with the standard principle of virtual work

$$\int_{\Omega} \boldsymbol{\sigma} : \boldsymbol{\nabla}\boldsymbol{\eta} \, \mathrm{d}V = \int_{\Omega} \boldsymbol{f} \cdot \boldsymbol{\eta} \, \mathrm{d}V + \int_{\Gamma_\sigma} \boldsymbol{t}^{*} \cdot \boldsymbol{\eta} \, \mathrm{d}\Gamma, \tag{29}$$

where $\boldsymbol{\eta}$ denotes a regular test function $\boldsymbol{\eta}$, $\boldsymbol{f}$ the body loads and $\boldsymbol{t}^{*}$ the prescribed NEUMANN boundary conditions, the extension to domains exhibiting singular surfaces leads to (see [17])

$$-\int_{\Omega\setminus\partial_{\mathrm{s}}\Omega} (\mathrm{div}\boldsymbol{\sigma} + \boldsymbol{f}) \cdot \boldsymbol{\eta} \, \mathrm{d}V - \int_{\partial_{\mathrm{s}}\Omega} \underbrace{\boldsymbol{n} \cdot \left(\boldsymbol{\sigma}^{+} - \boldsymbol{\sigma}^{-}\right)}_{\text{traction equilibrium}} \cdot \boldsymbol{\eta} \, \mathrm{d}\Gamma + \int_{\Gamma_\sigma} (\boldsymbol{\nu} \cdot \boldsymbol{\sigma} - \boldsymbol{t}^{*}) \cdot \boldsymbol{\eta} \, \mathrm{d}\Gamma = 0. \tag{30}$$

Since $\boldsymbol{\eta}$ is assumed as a smooth function, the equilibrium condition (28) is not satisfied automatically (see e.g. [30]). Enforcing the traction continuity (23) in a weak sense and considering the singular distribution of the localization zone with the area A_{s} leads to

$$\frac{1}{V} \int_{\Omega} (\boldsymbol{m} \otimes \boldsymbol{n})^{\mathrm{sym}} : \boldsymbol{\sigma} \, \mathrm{d}\Omega = \frac{1}{A_{\mathrm{s}}} \int_{\partial_{\mathrm{s}}\Omega} q(\alpha) \, \mathrm{d}\Gamma. \tag{31}$$

Equation (31) can be equivalently written in the form

$$\int_\Omega \hat{\boldsymbol{G}} : \boldsymbol{\sigma} \, \mathrm{d}\Omega = 0 \tag{32}$$

with the second order tensor

$$\hat{\boldsymbol{G}} = -\frac{A_\mathrm{s}}{V} \; (\boldsymbol{m} \otimes \boldsymbol{n})^{\mathrm{sym}} + (\boldsymbol{m} \otimes \boldsymbol{n})^{\mathrm{sym}} \; \delta_\mathrm{s}. \tag{33}$$

For a detailed derivation of this equivalence we refer to [27]. Equation (32) has a format analogous to the L_2-orthogonality condition in the enhanced strain concept [41]. Since, in general $\hat{\boldsymbol{G}} \neq \boldsymbol{G}$, this formulation corresponds to a PETROV-GALERKIN type approach resulting in a non-symmetric stiffness matrix. Hence, it is not identical to the symmetric EAS concept originally proposed by SIMO & RIFAI [41] (see also the respective discussion in [42]).

As alluded before, the localization surface must cross the respective GAUSS point and its direction can be different in each of the integration points. More precisely, the localization zones associated with the respective GAUSS points are independent of neighboring failure surfaces. As a consequence Equation (32) has to be postulated for each of the active integration points. Assuming a constant rate of the displacement jump along the localization band ($\dot{\zeta} \neq \dot{\zeta}(\boldsymbol{x})$, $\boldsymbol{m} \neq \boldsymbol{m}(\boldsymbol{x})$) as well as a spatially fixed orientation of the localization surface given by the vector $\boldsymbol{n}$ ($\boldsymbol{n} \neq \boldsymbol{n}(\boldsymbol{x})$) at a respective integration point i, Equation (31) can be simplified to

$$\frac{1}{V} \int_\Omega \left(\boldsymbol{m}^{(i)} \otimes \boldsymbol{n}^{(i)}\right)^{\mathrm{sym}} : \boldsymbol{\sigma}^{(i)} \, \mathrm{d}\Omega = q^{(i)}(\alpha^{(i)}). \tag{34}$$

Inserting the integrated form of Equations $(9)_1$, using a backward EULER integration scheme within the time interval $[t_n, t_{n+1}]$, together with the kinematic equations (4) and (20), the left hand side of Equation(31) can be written at t_{n+1} as

$$\begin{aligned}
&\frac{1}{V} \int_\Omega \left(\boldsymbol{m}_{n+1}^{(i)} \otimes \boldsymbol{n}_{n+1}^{(i)}\right)^{\mathrm{sym}} : \boldsymbol{\sigma}_{n+1}^{(i)} \, \mathrm{d}\Omega \\
= \; & \left(\boldsymbol{m}_{n+1}^{(i)} \otimes \boldsymbol{n}_{n+1}^{(i)}\right)^{\mathrm{sym}} : \left[\frac{1}{V} \int_\Omega \mathbb{C} : \left(\nabla^{\mathrm{sym}} \bar{\boldsymbol{u}}_{n+1}^{(i)} - \tilde{\boldsymbol{\varepsilon}}_n^{(i)} - \boldsymbol{G}_{n+1}^{(i)}(\boldsymbol{x}) \; \Delta\zeta_{n+1}^{(i)}\right) \, \mathrm{d}\Omega\right] \\
= \; & \left(\boldsymbol{m}_{n+1}^{(i)} \otimes \boldsymbol{n}_{n+1}^{(i)}\right)^{\mathrm{sym}} : \underbrace{\mathbb{C} : (\nabla^{\mathrm{sym}} \bar{\boldsymbol{u}}_{n+1}^{(i)} - \tilde{\boldsymbol{\varepsilon}}_n^{(i)} - \underbrace{\frac{1}{V} \int_\Omega \boldsymbol{G}_{n+1}^{(i)}(\boldsymbol{x}) \mathrm{d}\Omega}_{\bar{\boldsymbol{G}}_{n+1}^{(i)}} \; \Delta\zeta_{n+1}^{(i)})}_{\boldsymbol{\sigma}_{n+1}^{(i)}},
\end{aligned} \tag{35}$$

where the notation $(\bullet)_{n+1} = (\bullet)(t = t_{n+1})$ and $\Delta(\bullet)_{n+1} = (\bullet)_{n+1} - (\bullet)_n$ for a variable $(\bullet)$ at the pseudo time t was used. $\nabla^{\mathrm{sym}}\boldsymbol{u}$ and $\tilde{\boldsymbol{\varepsilon}}$, respectively, are computed at the respective GAUSS-point associated with a surface of discontinuity and the integration refers to the domain of the finite element. Hence, in Equation (35) only the second order tensor $\boldsymbol{G}$ depends on $\boldsymbol{x}$. From Equation (21) follows that

$$\bar{\boldsymbol{G}} = \frac{1}{V} \int_\Omega \boldsymbol{G}^{(i)}(\boldsymbol{x}) \, \mathrm{d}V = \left(\overline{\boldsymbol{\nabla}\varphi} \otimes \boldsymbol{m}\right)^{\mathrm{sym}} \tag{36}$$

with

$$\overline{\boldsymbol{\nabla}\varphi} = \frac{1}{V}\int_{\Omega} \boldsymbol{\nabla}\varphi(\boldsymbol{x})\,\mathrm{d}\Omega. \tag{37}$$

Setting, as a particular choice for the tensor $\boldsymbol{G}$

$$\boldsymbol{G} \equiv \bar{\boldsymbol{G}}, \tag{38}$$

it follows from Equations (35) and (34) that the weak form of equilibrium according to Equation (34)

$$-\frac{1}{A_{\mathrm{s}}}\int_{\Omega} \hat{\boldsymbol{G}} : \boldsymbol{\sigma}\,\mathrm{d}V = (\boldsymbol{m}\otimes\boldsymbol{n})^{\mathrm{sym}} : \boldsymbol{\sigma}(\bar{\boldsymbol{G}}) - q(\zeta) = 0 \tag{39}$$

is identical to the strong form at the respective GAUSS-point.

4.2 Algorithmic formulation considering rotating localization surfaces

At the end of a time interval $[t_n, t_{n+1}]$, the updated state of stresses and of the softening parameter q are computed as

$$\begin{aligned} \boldsymbol{\sigma}_{n+1} &= \mathbb{C} : \left(\boldsymbol{\nabla}^{\mathrm{sym}}\bar{\boldsymbol{u}}_{n+1} - \tilde{\boldsymbol{\varepsilon}}_{n+1}\right), \\ q_{n+1} &= q_{n+1}\left(\alpha_{n+1}\right). \end{aligned} \tag{40}$$

Equation $(40)_1$ is defined for $\boldsymbol{x} \in \Omega^+ \cup \Omega^-$. With the definition of a trial state

$$\boldsymbol{\sigma}^{\mathrm{tr}}_{n+1} = \mathbb{C} : \left(\boldsymbol{\nabla}^{\mathrm{sym}}\bar{\boldsymbol{u}}_{n+1} - \tilde{\boldsymbol{\varepsilon}}_{n}\right), \tag{41}$$

together with the integrated form of Equation (20), Equation $(40)_1$ can be re-formulated as

$$\boldsymbol{\sigma}_{n+1} = \boldsymbol{\sigma}^{\mathrm{tr}}_{n+1} - \mathbb{C} : \Delta\tilde{\boldsymbol{\varepsilon}}_{n+1} = \boldsymbol{\sigma}^{\mathrm{tr}}_{n+1} - \mathbb{C} : \boldsymbol{G}_{n+1}\,\Delta\zeta_{n+1}. \tag{42}$$

The loading condition associated with the trial state is given as

$$\phi^{\mathrm{tr}}_{n+1}(\boldsymbol{\sigma}^{\mathrm{tr}}_{n+1}, q^{\mathrm{tr}}_{n+1}) > 0 \tag{43}$$

with $q^{\mathrm{tr}}_{n+1} = q(\alpha_n)$.

The updated state of enhanced strains $\tilde{\boldsymbol{\varepsilon}}_{n+1}$ and of the internal variables α_{n+1} are obtained from applying a backward EULER integration scheme to the evolution equations (20) and $(9)_3$ as

$$\begin{aligned} \tilde{\boldsymbol{\varepsilon}}_{n+1} &= \tilde{\boldsymbol{\varepsilon}}_{n} + \boldsymbol{G}_{n+1}\,\Delta\zeta_{n+1}, \\ \alpha_{n+1} &= \alpha_n + \Delta\alpha_{n+1} = \alpha_n + |\Delta\zeta_{n+1}|. \end{aligned} \tag{44}$$

The failure criterion ϕ_{n+1} evaluated at t_{n+1} is given as

$$\phi_{n+1} = (\boldsymbol{m}_{n+1}\otimes\boldsymbol{n}_{n+1}) : \boldsymbol{\sigma}_{n+1} - q_{n+1} = 0. \tag{45}$$

In contrast to previous formulations of the Strong Discontinuity Approach, the discontinuity surface may now rotate during loading. This is accomplished by letting the tensor $\boldsymbol{G}$ change during the loading process. Linearization of Equation (40) within a particular step of the return mapping algorithm iteration yields [43],

$$\begin{aligned} \mathrm{d}\boldsymbol{\sigma}_{n+1} &= -\,\mathbb{C} : \mathrm{d}\tilde{\boldsymbol{\varepsilon}}_{n+1}, \\ \mathrm{d}q_{n+1} &= -\,D_{n+1}\,\mathrm{d}\alpha_{n+1} \end{aligned} \tag{46}$$

with D=-$\partial q/\partial\alpha$. In the k-th iteration, linearization of the residuals of Equation (44), defined as

$$\begin{aligned} \boldsymbol{R}^{\boldsymbol{\varepsilon}} &= -\tilde{\boldsymbol{\varepsilon}}_{n+1} + \tilde{\boldsymbol{\varepsilon}}_n + \boldsymbol{G}_{n+1}\,\Delta\zeta_{n+1}, \\ R^{\alpha} &= -\alpha_{n+1} + \alpha_n + |\Delta\zeta_{n+1}|, \end{aligned} \tag{47}$$

results, in full analogy to standard elastoplastic models, in the algebraic system of equations

$$\begin{aligned} &\boldsymbol{R}^{\boldsymbol{\varepsilon}} + \mathrm{d}\boldsymbol{R}^{\boldsymbol{\varepsilon}} = \boldsymbol{0}, \\ &R^{\alpha} + \mathrm{d}R^{\alpha} = 0, \\ &\phi_{n+1} + \mathrm{d}\phi_{n+1} = 0. \end{aligned} \tag{48}$$

Linearization of Equations (47) yields

$$\underbrace{\begin{bmatrix} \mathrm{d}\boldsymbol{R}^{\boldsymbol{\varepsilon}} \\ \mathrm{d}R^{\alpha} \end{bmatrix}}_{\mathrm{d}\boldsymbol{R}} = \underbrace{\begin{bmatrix} \boldsymbol{\Xi}_{n+1}^{-1} & \boldsymbol{0} \\ 0 & D^{-1} \end{bmatrix}}_{\boldsymbol{A}^{-1}} \underbrace{\begin{bmatrix} \mathrm{d}\boldsymbol{\sigma}_{n+1} \\ \mathrm{d}q_{n+1} \end{bmatrix}}_{\boldsymbol{\Delta}} + \mathrm{d}\Delta\zeta_{n+1} \underbrace{\begin{bmatrix} \boldsymbol{G}_{n+1} \\ \mathrm{sign}\,[\mathrm{d}\Delta\zeta_{n+1}] \end{bmatrix}}_{\boldsymbol{\nabla}M}. \tag{49}$$

In Equation (49), $\boldsymbol{\Xi}$ denotes the algorithmic moduli

$$\boldsymbol{\Xi}_{n+1}^{-1} = \mathbb{C}^{-1} + \mathbb{G}_{n+1}^{\mathrm{sym}}. \tag{50}$$

The tensor $\mathbb{G}_{n+1}^{\mathrm{sym}}$ is obtained from linearization of $\boldsymbol{G}_{n+1}$ with respect to the stress tensor. Since, according to Equations (38) and (36), $\boldsymbol{G}$ depends on $\boldsymbol{m}$, the tensor $\mathbb{G}_{n+1}^{\mathrm{sym}}$ is computed as

$$\mathbb{G}_{n+1}^{\mathrm{sym}} = \Delta\zeta_{n+1} \left(\overline{\boldsymbol{\nabla}\varphi} \otimes \frac{\partial \boldsymbol{m}_{n+1}}{\partial \boldsymbol{\sigma}_{n+1}} \right)^{\mathrm{sym}}, \quad \text{with:} \quad [\,\mathbb{G}\,]^T_{ijkl} = [\,\mathbb{G}\,]_{jikl}\,. \tag{51}$$

For the special case of mode I failure, where $\boldsymbol{n}$ and $\boldsymbol{m}$ coincide with a principal axis of the stress tensor, the derivative $\partial\boldsymbol{n}/\partial\boldsymbol{\sigma}$ is given in Appendix A.

From inserting the consistency condition

$$\mathrm{d}\phi_{n+1} = \underbrace{\begin{bmatrix} \boldsymbol{m}_{n+1} \otimes \boldsymbol{n}_{n+1} \\ -1 \end{bmatrix}}_{\boldsymbol{\nabla}\phi} \cdot \underbrace{\begin{bmatrix} \mathrm{d}\boldsymbol{\sigma}_{n+1} \\ \mathrm{d}q_{n+1} \end{bmatrix}}_{\boldsymbol{\Delta}} \tag{52}$$

into Equation $(48)_3$, the change of the amplitude of the displacement jump during an iteration cycle is obtained as

$$\mathrm{d}\Delta\zeta_{n+1} = \frac{\phi_{n+1} - \boldsymbol{\nabla}\phi^T\,\boldsymbol{A}\,\boldsymbol{R}}{\boldsymbol{\nabla}\phi^T\,\boldsymbol{A}\,\boldsymbol{\nabla}M}. \tag{53}$$

At a converged state, characterized by $\boldsymbol{R} = \boldsymbol{0}$ and $\phi = 0$, the algorithmic tangent moduli are computed from the consistent linearization of the algorithm at t_{n+1} as

$$\mathbb{C}^{\mathrm{ep}} = \frac{\mathrm{d}\boldsymbol{\sigma}}{\mathrm{d}\boldsymbol{\nabla}^S\bar{\boldsymbol{u}}} = \boldsymbol{\Xi} - \frac{\left\{\boldsymbol{A}\,\boldsymbol{\nabla}M \otimes \boldsymbol{\nabla}\phi^T\,\boldsymbol{A}\right\}_{[11]}}{\boldsymbol{\nabla}\phi^T\,\boldsymbol{A}\,\boldsymbol{\nabla}M}, \tag{54}$$

where the abbreviation $\{\bullet\}_{[ij]}$ for the sub-matrix ij has been used. It should be noted, that the format of Equation (54) generally holds for a broad range of elastoplastic as well as damage models [26] and is not restricted to the specific class of elastoplastic models investigated in Section 3.

For the special case of the RANKINE type failure surface (19), the algorithmic tangent operator $\mathbb{C}^{\mathrm{ep}}$ is obtained as

$$\mathbb{C}^{\mathrm{ep}} = \boldsymbol{\Xi}_{n+1} - \frac{\boldsymbol{\Xi}_{n+1} : \boldsymbol{G}_{n+1} \otimes [\boldsymbol{n}_{n+1} \otimes \boldsymbol{n}_{n+1}] : \boldsymbol{\Xi}_{n+1}}{[\boldsymbol{n}_{n+1} \otimes \boldsymbol{n}_{n+1}] : \boldsymbol{\Xi}_{n+1} : \boldsymbol{G}_{n+1} - D_{n+1}\,\mathrm{sign}\,[\mathrm{d}\Delta\zeta_{n+1}]}. \tag{55}$$

Although formally identical to the algorithmic tangent operator obtained for continuum elastoplastic models, a comparison between the tangent moduli (54) and the respective formulation for the continuum case reveals that, although an associated flow rule is used, linearization results in a non-symmetric 4th-order tensor $\mathbb{C}^{\mathrm{ep}}$. Only for special cases (i.e. $\boldsymbol{G} = c\partial_{\boldsymbol{\sigma}}\phi$, $c \in \mathbb{R}$) a symmetric tangent operator is recovered.

It should be noted, that the proposed model affects only the material routines and not, as in most of the previous implementations of SDA-based models, the finite element level. Therefore, any finite element subroutine for non-associated plasticity models can directly be used as the framework for the implementation of the present SDA-based elastoplastic model.

4.3 Fixed localization surfaces

Fixed orientations of the discontinuity surface after onset of failure can be considered as a special case of the more general rotating formulation. In this case, the second order tensor $\boldsymbol{G}$ used in Equation $(44)_1$ is constant. Hence, $\frac{\partial \boldsymbol{n}_{n+1}}{\partial \boldsymbol{\sigma}_{n+1}} = \mathbf{0}$ and $\mathbb{G}^{\mathrm{sym}}_{n+1} = \mathbf{0}$. Consequently, the identity $\boldsymbol{\Xi}_{n+1} = \mathbb{C}$ holds.

The jump of the displacement field is now formulated in terms of a local coordinate system as

$$[\boldsymbol{u}] = \zeta^{(n)}\, \boldsymbol{n} + \zeta^{(m,1)}\, \boldsymbol{m}^{(1)} + \zeta^{(m,2)}\, \boldsymbol{m}^{(2)}, \tag{56}$$

with

$$\boldsymbol{n} \cdot \boldsymbol{m}^{(i)} = 0 \quad \forall i \in \{1,2\} \quad \text{and} \quad \boldsymbol{m}^{(1)} \cdot \boldsymbol{m}^{(2)} = 0. \tag{57}$$

If only mode-I fracture is considered, assuming no residual shear stiffness along the crack surfaces, the normal component of the traction vector is governed by the condition

$$\phi(\boldsymbol{\sigma}, \alpha) = (\boldsymbol{n} \otimes \boldsymbol{n}) : \boldsymbol{\sigma} - q(\alpha) \qquad \text{with} \quad \dot{\alpha} = |\dot{\zeta}^{(n)}| \tag{58}$$

while for the tangential (shear) components

$$\left(\boldsymbol{m}^{(1)} \otimes \boldsymbol{n}\right) : \boldsymbol{\sigma} = 0 \quad \text{and} \quad \left(\boldsymbol{m}^{(2)} \otimes \boldsymbol{n}\right) : \boldsymbol{\sigma} = 0, \tag{59}$$

is assumed to hold. Equations (59) are equivalent to the assumption of a shear retention factor set to zero.

Accordingly, the tensor of enhanced strains $\tilde{\boldsymbol{\varepsilon}}$ is decomposed into parts corresponding to the normal and to the tangential displacements, respectively:

$$\tilde{\boldsymbol{\varepsilon}} = \tilde{\boldsymbol{\varepsilon}}^{(n)} + \tilde{\boldsymbol{\varepsilon}}^{(m,1)} + \tilde{\boldsymbol{\varepsilon}}^{(m,2)}. \tag{60}$$

These three individual parts are related to the respective components of the displacement jumps according to Equations (20) and (21):

$$\begin{aligned} \tilde{\boldsymbol{\varepsilon}}^{(n)} &= \left(\boldsymbol{n} \otimes \overline{\boldsymbol{\nabla}\varphi}\right)\, \zeta^{(n)}, \\ \tilde{\boldsymbol{\varepsilon}}^{(m,i)} &= \left(\boldsymbol{m}^{(i)} \otimes \overline{\boldsymbol{\nabla}\varphi}\right)\, \zeta^{(m,i)}, \quad \forall i \in \{1,2\}. \end{aligned} \tag{61}$$

In the context of the algorithmic formulation of the SDA-based fixed crack model, the increment of the tensor $\tilde{\boldsymbol{\varepsilon}}$ is obtained from the application of a backward EULER integration scheme as

$$\Delta\tilde{\boldsymbol{\varepsilon}}_{n+1} = \left(\boldsymbol{n} \otimes \overline{\boldsymbol{\nabla}\varphi}\right)\, \Delta\zeta^{(n)}_{n+1} + \sum_{i=1}^{2} \left(\boldsymbol{m}^{(i)} \otimes \overline{\boldsymbol{\nabla}\varphi}\right)\, \Delta\zeta^{(m,i)}_{n+1}. \tag{62}$$

The increments of the displacement jumps $\Delta\zeta^{(n)}_{n+1}$, $\Delta\zeta^{(m,i)}_{n+1}$ are computed from Equations (58), (59) together with (62) and Equation (42) by means of the general multisurface closest point projection iteration scheme (see e.g. [43]). The two-dimensional algorithmic formulation of the SDA-based fixed crack model is completely described in Appendix B.

4.4 Comparative assessment of fixed and rotating localization formulations

This subsection contains a numerical study of a notched concrete beam analyzed by means of the rotating as well as the fixed formulation of the SDA-based softening Rankine-model as described in Section 4. The geometry, the loading and boundary conditions of the beam and the material parameters are contained in Figure 7. The dimensions as well as the material parameters are chosen according to [44]. The finite element discretization by means of 840 bilinear plane stress elements is illustrated in Figure 8a. Loading on top of the beam was applied by incrementally increasing nodal displacements along the width of the loading platen.

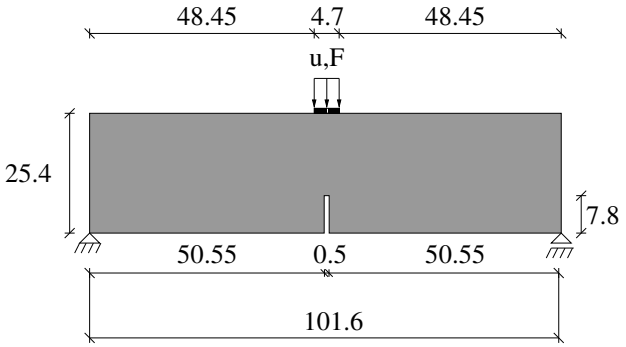

t	=	0.127	[m]
E	=	$4.36 \cdot 10^3$	[KN/cm^2]
ν	=	0.2	
f_{tu}	=	0.4	[KN/cm^2]
$\mathcal{G}_{\mathrm{f}}$	=	$1.195 \cdot 10^{-3}$	[KN cm/cm^2]

Figure 7: Numerical study of a notched concrete beam: Dimensions (in [cm]) and material parameters

The softening behavior after onset of cracking is assumed to follow the exponential law

$$q(\alpha) = f_{\mathrm{tu}} \, \exp\left[-\alpha \, \frac{f_{\mathrm{tu}}}{\mathcal{G}_{\mathrm{f}}}\right], \tag{63}$$

where $\mathcal{G}_{\mathrm{f}}$ denotes the specific fracture energy of concrete in tension and f_{tu} is the uniaxial tensile strength of concrete. Convergence is checked according to the criterion

$$\frac{||\boldsymbol{r}_i - \boldsymbol{r}_e||_\infty}{||\boldsymbol{r}_e||_\infty} < 10^{-6}, \tag{64}$$

where $\boldsymbol{r}_i$ ($\boldsymbol{r}_e$) is the vector of internal (external) forces.

Figure 8a contains the deformed structure as obtained from an analysis using the rotating crack formulation of the SDA-model according to Subsection 4.2. Figure 8b contains load-displacement-diagrams resulting from the fixed as well as from the rotating formulation. While in the pre-peak regime both formulations yield almost identical results, larger deviations are observed in the post-peak branch. In contrast to the rotating formulation, no convergence was obtained for the analysis based on the fixed crack model already at a relatively early stage after surpassing the ultimate load.

For a more detailed investigation of the convergence problems of the analysis based on the fixed crack approach, Figure 9 shows enlarged plots of the area in the vicinity of the crack tip including the directions of the maximum principle stress as obtained from the rotating and the fixed formulation. According to both analyses, the direction of the maximum principal stress in the uncracked part of the beam along the symmetry line in the vicinity of the crack tip is predicted orthogonal to (and not aligned with) the axis of the beam. In both models, this direction defines the normal vector $\boldsymbol{n}$ of a crack aligned with (and not orthogonal to) the axis of the beam. In contrast to the rotating formulation, however, this direction of the crack is held

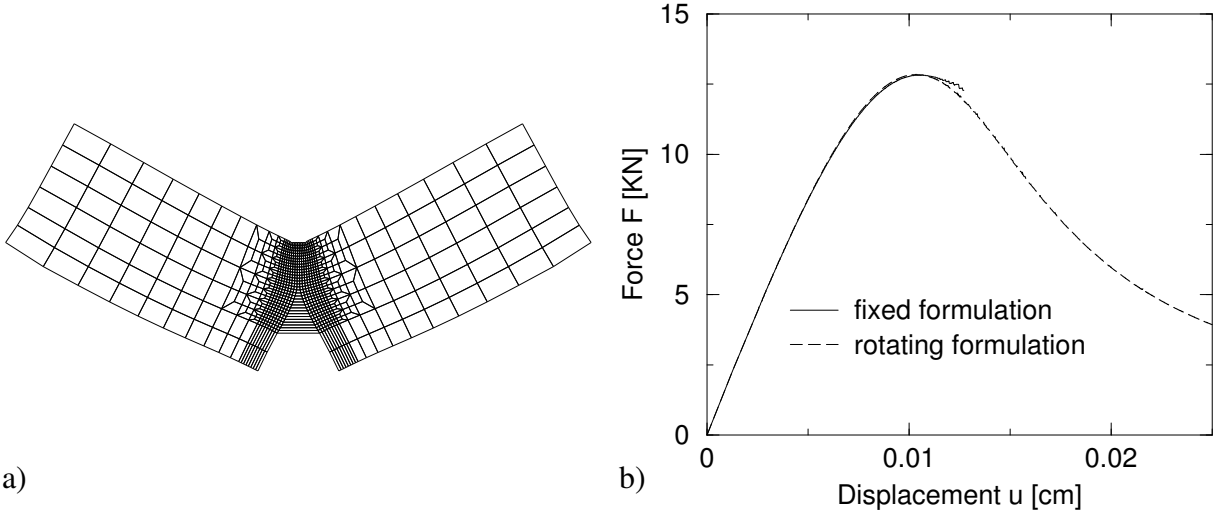

Figure 8: Numerical study of a notched concrete beam: a) Deformed structure at $u = 0.0127$ cm obtained from the rotating crack formulation (2000-fold magnification of displacements), b) load-displacement-diagrams obtained from the fixed and the rotating crack formulation

constant in the fixed crack formulation during subsequent loading. Hence, a wrong orientation of the crack is predicted at this stage of the loading. According to the rotating crack model, however, the direction of the maximum stress rotates from a vertical into a horizontal position during the further opening of the crack. Since in the rotating crack formulation the normal vector $\boldsymbol{n}$ rotates with the maximum tensile stress, a correct crack orientation is predicted. This stress locking effect, previously documented e.g. by JIRASEK & ZIMMERMANN [19], is also present if quadratic elements are used. It could be also eliminated if the SDA-based fixed crack formulation would allow for intersecting cracks.

5 NUMERICAL EXAMPLE

The SDA formulation for 3D hexahedral finite elements as proposed in Section 4 is employed for the numerical analysis of a steel anchor embedded within a block of concrete which is subjected to a shear force. In the example, the anchor is located in the vicinity of one of the surfaces of the block of concrete. This problem has been previously analyzed experimentally and numerically by HOFMANN,ELIGEHAUSEN & OZBOLT [45]. The geometry and the material parameters of the block of concrete (74 cm$\times$42 cm$\times$37 cm) and the steel anchor (cross sectional area 2.5×2.5 cm), together with the support conditions are contained in Figure 10. Since the primary focus of this numerical example is to demonstrate the applicability of the proposed 3D-model for concrete cracking, only tensile cracking is taken into account, although the experiments documented in [45] indicate a relatively strong influence of the compression strength on the maximum load.

The SDA-based RANKINE-model, using the rotating crack approach according to Subsection 4.2, is used in conjunction with a hyperbolic softening law

$$q(\alpha) = f_{\mathrm{tu}} \frac{1}{\left(1 - \frac{\alpha}{\alpha_{\mathrm{u}}}\right)^2}, \tag{65}$$

with $\alpha_{\mathrm{u}} = \mathcal{G}_{\mathrm{f}}/f_{\mathrm{tu}}$. $\mathcal{G}_{\mathrm{f}}$ denotes the specific fracture energy of concrete. For the modeling of the steel HOOKE's law is adopted. Frictionless contact is assumed between the steel anchor and the

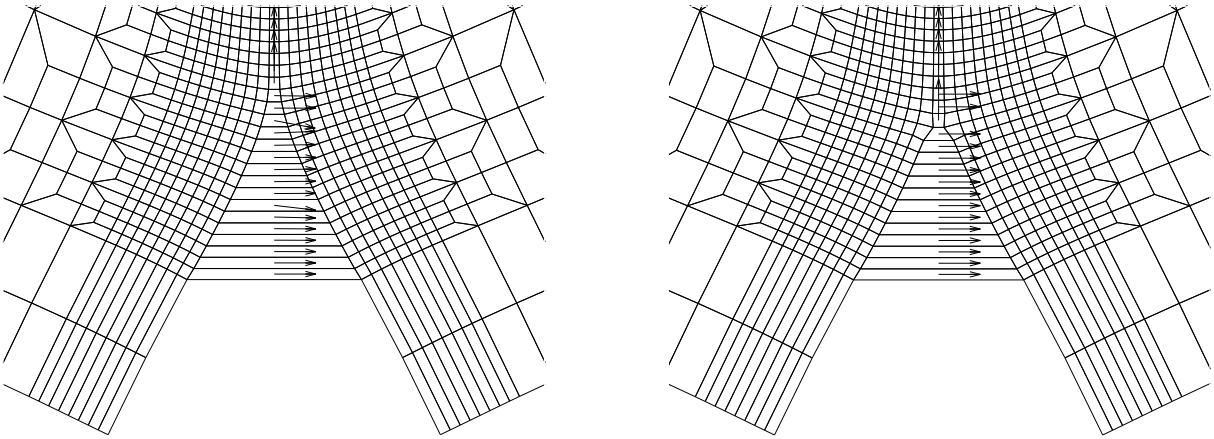

a) b)

Figure 9: Numerical study of a notched concrete beam: Deformed structure in the vicinity of the crack tip at $u = 0.0127$ cm including the principle directions of the maximum principle stress (2000-fold magnification of displacements): a) Rotating crack formulation b) fixed crack formulation

concrete.

Figure 11 illustrates two different discretizations of the block of concrete and the steel anchor, containing 711 and 1222 tri-linear elements, respectively, Because of symmetry of the geometry and the boundary conditions with respect to one axis, only one half of the concrete block and the anchor bolt was discretized. In the analyses, the vertical displacement of the head stud was increased by steps of 0.0020513 mm. Convergence is checked according to the criterion (64).

The load-displacement diagrams resulting from the analyses of the coarse and the fine mesh are shown in Figure 12. From the investigated finite element discretizations a maximum loading of approximately 18.2 kN (coarse mesh) and 19.4 kN (fine mesh) is obtained. Only a minor influence of the chosen discretization on the peak load and the post-peak response is reflected in the diagrams. The fine mesh yields an ultimate load approximately 7 % larger compared to the coarse mesh. This reflects a (relatively small) influence of the discretization on the topology of the crack formation. The maximum shear load obtained from the numerical analyses of only half of the structure reported in [45] are ranging between 14 kN (for the compressive strength of concrete chosen as f_{cu}= 15 MPa) and 16.5 kN (for f_{cu}= 35 MPa). The respective experimental data are ranging between 13 and 16 kN [45]. Since failure in compression has not been been considered in the present analyses, a larger value for the computed ultimate load is expected.

Figures 13 and 14 contain the distribution of the internal variable α, which reflects the state of cracking, obtained from the coarse mesh (Figure 13) and from the fine mesh (Figure 14). As expected, a better resolution of the localized fracture zone is obtained from the fine mesh. The shape of this failure zone, however, is only marginally affected by the mode of discretization. For both discretizations the failure mode agrees reasonably well with the experimentally observed crack patterns. After the crack tips have reached the front surface of the concrete block, a closed fracture surface has formed.

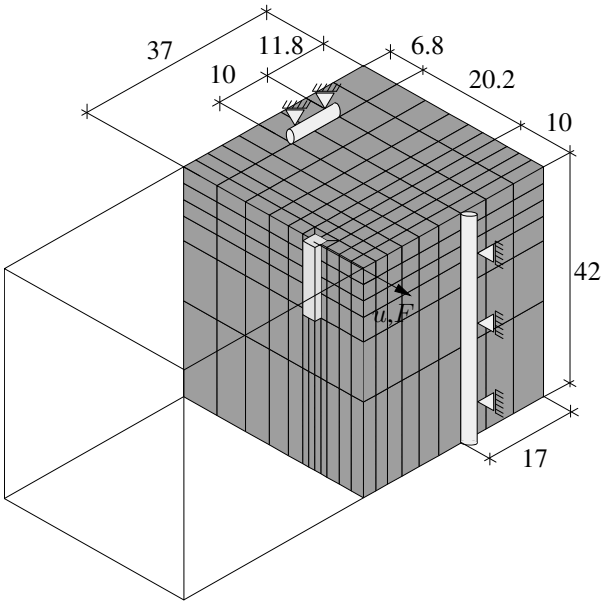

Concrete:

E	=	3500	[kN/cm^2]
ν	=	0.2	
$\mathcal{G}_\mathrm{f}$	=	$7.5{\cdot}10^{-4}$	[kN cm/cm^2]
f_tu	=	0.25	[kN/cm^2]

Steel:

E	=	21000	[kN/cm^2]
ν	=	0.3	

Figure 10: 3D finite element analysis of an anchor subjected to shear loading: Dimensions (in [cm]) and material parameters

6 CONCLUSIONS

A formulation of the so-called Strong Discontinuity Approach (SDA) suitable for large scale two- and three-dimensional failure analyses of elastoplastic solids has been presented in the paper. The proposed formulation allows implementations within 2D and 3D finite elements using arbitrary orders of the displacement interpolations. The extension of the embedded discontinuity concept to finite elements which are not characterized by a constant strain field is achieved by assuming planar localization surfaces located in those integration points, in which the onset of localization is signalled according to the underlying failure criterion and by the weak enforcement of the traction continuity along the discontinuity surface.

A continuum approach was followed in the sense that the traction separation law is obtained from the projection of an elastoplastic continuum model onto the localization surface. The proposed formulation results in a computational algorithm which is formally identical to standard non-associative plasticity models. The enhanced strains are added only at the integration-point level, leaving the element routines unaffected. Since the parameter defining the amplitude of the displacement jump is determined at the material level, using the standard return-mapping algorithm, the implementation of the algorithm only requires minor modifications of material subroutines designed for standard plasticity models.

As an alternative to the assumption of a fixed localization surface a dependence of the localization surface on the deformation in analogy to plasticity-based smeared crack models is taken into account in the proposed model. The algorithmic formulations were given for both rotating and fixed SDA-based models. From a comparative numerical study using a fixed as well as a rotating crack model it was shown, that, allowing for rotations of the localization zone such as cracks, reduces the effect of stress locking and considerably improves the robustness of failure analyses. The efficiency and robustness of the model was also demonstrated by means of a 3D analysis of a steel anchor embedded within a concrete block subjected to shear loading.

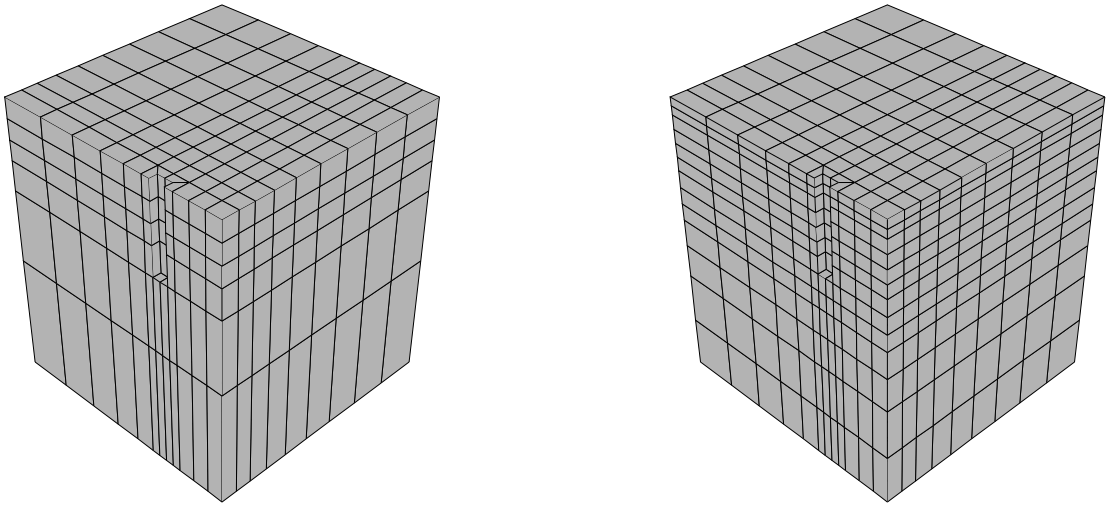

a) b)

Figure 11: Finite element discretizations used for the analysis of the anchor shear test: a) Coarse mesh (711 tri-linear elements), b) fine mesh (1222 tri-linear elements)

APPENDIX A

This Appendix contains the determination of the derivative $\partial \boldsymbol{n}/\partial \boldsymbol{\sigma}$ required for the computation of the algorithmic tangent moduli for RANKINE based models using the proposed rotating formulation of the embedded discontinuity approach according to Subsection 4.2.

Let $\boldsymbol{\sigma}$ be a symmetric second order tensor. The spectral decomposition of this tensor is defined by the eigenvalue problem

$$\boldsymbol{\sigma} \cdot \boldsymbol{n} = \lambda \, \boldsymbol{n}, \tag{66}$$

where λ represents an eigenvalue and $\boldsymbol{n}$ is a corresponding eigenvector. Differentiation of Equation (66) with respect to $\boldsymbol{\sigma}$ leads to

$$\mathbb{I} \cdot \ \boldsymbol{n} + \boldsymbol{\sigma} \cdot \frac{\partial \boldsymbol{n}}{\partial \boldsymbol{\sigma}} = \lambda \, \frac{\partial \boldsymbol{n}}{\partial \boldsymbol{\sigma}} + \frac{\partial \lambda}{\partial \boldsymbol{\sigma}} \otimes \boldsymbol{n}, \tag{67}$$

with the 4th order identity tensor $\mathbb{I}$. Since Equation (67) contains the two unknown tensors $\partial \boldsymbol{n}/\partial \boldsymbol{\sigma}$, $\partial \lambda/\partial \boldsymbol{\sigma}$, the normalizing condition

$$\boldsymbol{n} \cdot \boldsymbol{n} = 1 \quad \Rightarrow \quad \boldsymbol{n} \cdot \mathrm{d}\boldsymbol{n} = 0 \tag{68}$$

must also be used. Rewriting Equations (67) and (68) in matrix form yields

$$\underbrace{\begin{bmatrix} \boldsymbol{n}^T & 0 \\ \boldsymbol{\sigma} - \lambda \, \mathbf{1} & -\boldsymbol{n} \end{bmatrix}}_{\boldsymbol{A}} \begin{bmatrix} \dfrac{\partial \boldsymbol{n}}{\partial \sigma_{ij}} \\ \dfrac{\partial \lambda}{\partial \sigma_{ij}} \end{bmatrix} = \begin{bmatrix} 0 \\ -\dfrac{\partial \boldsymbol{\sigma}}{\partial \sigma_{ij}} \cdot \boldsymbol{n} \end{bmatrix}. \tag{69}$$

From Equation (69), after inverting $\boldsymbol{A}$, the derivative $\partial \boldsymbol{n}/\partial \boldsymbol{\sigma}$ can be computed. The matrix $\boldsymbol{A}$ is singular if and only if λ is a repeated eigenvalue of the symmetric tensor $\boldsymbol{\sigma}$. In this case the eigenvalues are perturbed by a small numerical parameter.

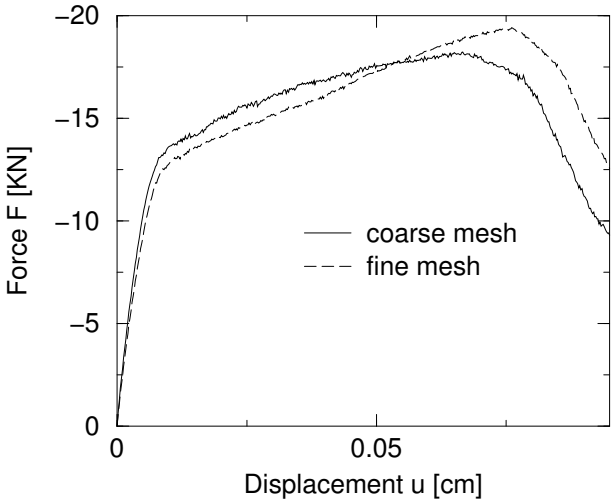

Figure 12: 3D finite element analysis of an anchor subjected to shear loading: Load-displacement diagrams $u - F$

APPENDIX B

This Appendix contains the numerical implementation of the SDA-based fixed crack model described in Subsection 4.3 in a two-dimensional context. Hence, $\boldsymbol{m}$ and $\zeta^{(m)}$ will be used instead of $\boldsymbol{m}^{(1)}$ and $\zeta^{(m,1)}$.

Inserting Equation (41) into Equation $(59)_1$, considering Equation (62), results in the following relation between the normal and the tangential component of the displacement jump:

$$\Delta\zeta_{n+1}^{(m)} = \frac{1}{g_{22}} \left[(\boldsymbol{m} \otimes \boldsymbol{n}) : \boldsymbol{\sigma}^{\mathrm{tr}} - g_{21}\, \Delta\zeta_{n+1}^{(n)} \right]. \tag{70}$$

The components of the metric tensor $\boldsymbol{g}$ corresponding to the sub-space of active failure surfaces used in Equation (70) are given as

$$\begin{aligned} g_{11} &= (\boldsymbol{n} \otimes \boldsymbol{n}) : \mathbb{C} : \left(\boldsymbol{n} \otimes \overline{\boldsymbol{\nabla}\varphi}\right), & g_{21} &= (\boldsymbol{m} \otimes \boldsymbol{n}) : \mathbb{C} : \left(\boldsymbol{n} \otimes \overline{\boldsymbol{\nabla}\varphi}\right), \\ g_{12} &= (\boldsymbol{n} \otimes \boldsymbol{n}) : \mathbb{C} : \left(\boldsymbol{m} \otimes \overline{\boldsymbol{\nabla}\varphi}\right), & g_{22} &= (\boldsymbol{m} \otimes \boldsymbol{n}) : \mathbb{C} : \left(\boldsymbol{m} \otimes \overline{\boldsymbol{\nabla}\varphi}\right). \end{aligned} \tag{71}$$

If the loading condition associated with the trial state, $\phi^{\mathrm{tr}} > 0$, signals an opening of a crack, the stress tensor needs to be projected onto the updated failure surface ϕ_{n+1}. Substituting $\boldsymbol{\sigma}$ in Equation (58) by means of Equation (42) and inserting (70) results in a scalar equation for the increment of the displacement jump $\Delta\zeta^{(n)}$

$$\left[\boldsymbol{n} \otimes \boldsymbol{n} - \frac{g_{12}}{g_{22}}\, \boldsymbol{m} \otimes \boldsymbol{n} \right] : \boldsymbol{\sigma}^{\mathrm{tr}} - \left[g_{11} - \frac{g_{12}\, g_{21}}{g_{22}} \right] \Delta\zeta_{n+1}^{(n)} = q(\alpha_n + |\Delta\zeta_{n+1}^{(n)}|). \tag{72}$$

Equation (72) can be solved, e.g. by means of NEWTONs method.

The numerical implementation of the two-dimensional SDA-based fixed crack model is

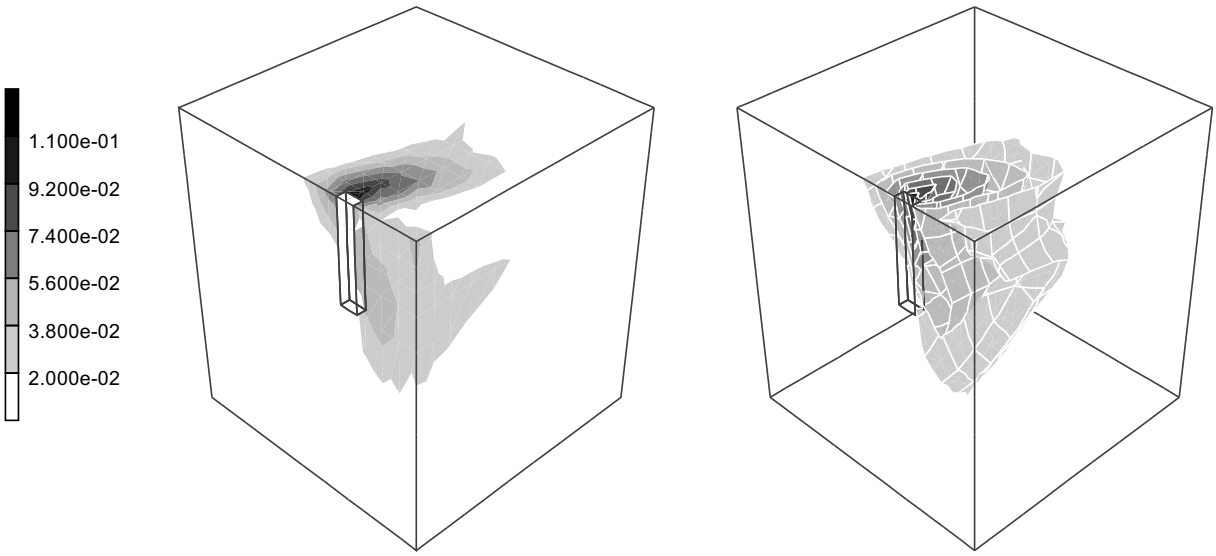

Figure 13: 3D finite element analysis of an anchor subjected to shear loading (coarse mesh): Distribution of the internal variable α representing the crack-width at $u_1 = 0.943598$ cm: a) Contours along the surfaces, b) iso-surfaces

completed with the computation of the algorithmic tangent moduli

$$\begin{aligned}\frac{\mathrm{d}\boldsymbol{\sigma}}{\mathrm{d}\boldsymbol{\nabla}^{\mathrm{s}}\bar{\boldsymbol{u}}} = \mathbb{C} \;&-\; \frac{\mathbb{C} : \left(\boldsymbol{n}\otimes\overline{\boldsymbol{\nabla}\varphi}\right)\otimes\left[\boldsymbol{n}\otimes\boldsymbol{n} - \frac{g_{12}}{g_{22}}\,\boldsymbol{m}\otimes\boldsymbol{n}\right] : \mathbb{C}}{\left[g_{11} - \frac{g_{12}\,g_{21}}{g_{22}}\right] - D\,\mathrm{sign}\Delta\zeta_{n+1}^{(n)}} \\ &-\; \frac{\mathbb{C} : \left(\boldsymbol{m}\otimes\overline{\boldsymbol{\nabla}\varphi}\right)\otimes\left(\boldsymbol{m}\otimes\boldsymbol{n}\right) : \mathbb{C}}{g_{22}} \\ &+\; \frac{\mathbb{C} : \left(\boldsymbol{m}\otimes\overline{\boldsymbol{\nabla}\varphi}\right)\otimes\left[\boldsymbol{n}\otimes\boldsymbol{n} - \frac{g_{12}}{g_{22}}\,\boldsymbol{m}\otimes\boldsymbol{n}\right] : \mathbb{C}}{\left[g_{11} - \frac{g_{12}\,g_{21}}{g_{22}}\right] - D\,\mathrm{sign}\Delta\zeta_{n+1}^{(n)}}\;\frac{g_{21}}{g_{22}}.\end{aligned} \tag{73}$$

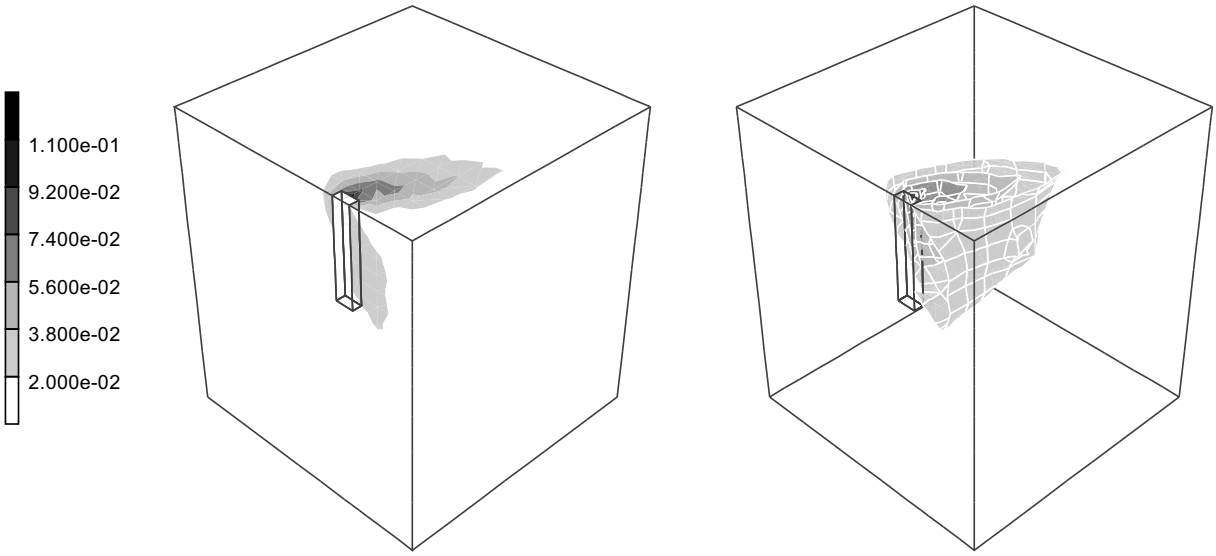

Figure 14: 3D finite element analysis of an anchor subjected to shear loading (fine mesh): Distribution of the internal variable α representing the crack-width at $u_1 = 0.943598$ cm: a) Contours along the surfaces, b) iso-surfaces

References

[1] J. Simo, J. Oliver, and F. Armero. An analysis of strong discontinuities induced by strain softening in rate-independent inelastic solids. *Computational Mechanics*, 12:277–296, 1993.

[2] R. De Borst. Some recent issues in computational failure mechanics. *International Journal for Numerical Methods in Engineering*, 52:63–95, 2001.

[3] G. Pijaudier-Cabot and Z.P. Bažant. Nonlocal damage theory. *Journal of Engineering Mechanics (ASCE)*, 113:1512–1533, 1987.

[4] G., Z.P. Bažant, and G. Pijaudier-Cabot. Nonlocal damage, localization, instability and convergence. *Journal of Applied Mechanics*, 55:287–293, 1988.

[5] H.B. Mühlhaus and E.C. Aifantis. A variational principle for gradient plasticity. *International Journal of Solids and Structures*, 28:845–857, 1991.

[6] R. De Borst and H.B. Mühlhaus. Gradient-dependent plasticity: Formulation and algorithmic aspects. *International Journal for Numerical Methods in Engineering*, 35:521–539, 1992.

[7] R. De Borst. Simulation of strain localization: A reappraisal of the Cosserat continuum. *Engineering Computations*, 8:317–332, 1991.

[8] P. Steinmann and K.J. Willam. Localization within the framework of micropolar elastoplasticity. In V. Mannl, J. Najar, and O. Brüller, editors, *Advances in continuum mechanics*, pages 296–313. Springer, Berlin-Heidelberg, 1991.

[9] I. Babuška and J.M. Melenk. The partition of unity method. *International Journal for Numerical Methods in Engineering*, 40:727–758, 1997.

[10] N. Moës, J. Dolbow, and T. Belytschko. A finite element method for crack growth without remeshing. *International Journal for Numerical Methods in Engineering*, 46:131–150, 1999.

[11] C. Johnson and R. Scott. A finite element method for problems in perfect plasticity using discontinuous trial functions. In W. Wunderlich, E. Stein, and K.J Bathe, editors, *Nonlinear finite element analysis in structural mechanics*, pages 307–324, 1981.

[12] T. Belytschko, J. Fish, and B.E. Engelmann. A finite element with embedded localization zones. *Computer Methods in Applied Mechanics and Engineering*, 70:59–89, 1988.

[13] E.N. Dvorkin, A. M. Cuitiño, and G. Gioia. Finite elements with displacement interpolated embedded localization lines insensitive to mesh size and distortions. *International Journal for Numerical Methods in Engineering*, 30:541–564, 1990.

[14] M. Klisinski, K. Runesson, and S.. Sture. Finite element with inner softening band. *Journal of Engineering Mechanics (ASCE)*, 117(3):575–587, 1991.

[15] A.R. Regueiro and R.I. Borja. A finite element method of localized deformation in frictional materials taking a strong discontinuity approach. *Finite Elements in Analysis and Design*, 33:283–315, 1999.

[16] J. Oliver, M. Cervera, and O. Manzoli. Strong discontinuities and continuum plasticity models: The strong discontinuity approach. *International Journal of Plasticity*, 15:319–351, 3 1999.

[17] J. Oliver. Modelling strong discontinuities in solid mechanics via strain softening constitutive equations Part 1: Fundamentals. Part 2: Numerical simulations. *International Journal for Numerical Methods in Engineering*, 39:3575–3623, 1996.

[18] F. Armero. Localized anisotropic damage of brittle materials. In D.R.J. Owen, E. Oñate, and E. Hinton, editors, *Computational Plasticity*, volume 1, pages 635–640, 1997.

[19] M. Jirásek and T. Zimmermann. Embedded crack model: Part I: Basic formulation, Part II: Combination with smeared cracks. *International Journal for Numerical Methods in Engineering*, 50:1269–1305, 2001.

[20] A.H. Berends, L.J. Sluys, and R. de Borst. Discontinuous modelling of mode-I failure. In D.R.J. Owen, E. Oñate, and E. Hinton, editors, *Computational Plasticity*, volume 1, pages 751–758, 1997.

[21] L.J. Sluys and A.H. Berends. 2D/3D modelling of crack propagation with embedded discontinuity elements. In R. de Borst, N. Bićanić, H. Mang, and G. Meschke, editors, *Computational Modelling of Concrete Structures, EURO-C98*, volume 1, pages 399–408. Elsevier, 1998.

[22] M. Petrangeli and J. Ožbolt. Smeared crack approaches - material modeling. *Journal of Engineering Mechanics (ASCE)*, 122(6):545–554, 1996.

[23] G. Hofstetter and H.A. Mang. *Computational Mechanics of Reinforced and Prestressed Concrete Structures*. Vieweg, Braunschweig, 1995.

[24] P. Feenstra and R. De Borst. A plasticity model and algorithm for mode-I cracking in concrete. *International Journal for Numerical Methods in Engineering*, 38:2509–2530, 1995.

[25] G. Meschke. Consideration of aging of shotcrete in the context of a 3-D viscoplastic material model. *International Journal for Numerical Methods in Engineering*, 39:3123–3143, 1996.

[26] J. Mosler and G. Meschke. An elastoplastic-damage model for quasi-brittle materials in the framework of the strong discontinuity approach. In R. De Borst, J. Mazars, G. Pijaudier-Cabot, and J.G.M. Van Mier, editors, *Fracture Mechanics of Concrete Structures IV*, volume 2, pages 817–822, 2001.

[27] F. Armero and K. Garikipati. Recent advances in the analysis and numerical simulation of strain localization in inelastic solids. In D.R.J. Owen, E Oñate, and E. Hinton, editors, *Proc., 4th Int. Conf. Computational Plasticity*, volume 1, pages 547–561, 1995.

[28] J. Mosler and G. Meschke. 3D FE analysis of cracks by means of the strong discontinuity approach. In E. Oñate, G. Bugeda, and B. Suárez, editors, *European Congress on Computational Methods in Applied Sciences and Engineering, CD-Rom*, 2000.

[29] J. Oliver and J. Simo. Modelling strong discontinuities in solid mechanics by means of strain softening constitutive equations. In H. Mang, N. Bićanić, and R. de Borst, editors, *Computational Modelling of concrete structures*, pages 363–372. Pineridge press, 1994.

[30] J. Simo and J. Oliver. A new approach to the analysis and simulation of strain softening in solids. In Z.P. Bažant, Z. Bittnar, M. Jirásek, and J. Mazars, editors, *Fracture and Damage in Quasibrittle Structures*, pages 25–39. E. &F.N. Spon, London, 1994.

[31] J. Oliver. Continuum modelling of strong discontinuities in solid mechanics using damage models. *Computational Mechanics*, 17(1-2):49–61, 12 1995.

[32] K. Garikipati. *On strong discontinuities in inelastic solids and their numerical simulation*. PhD thesis, Stanford University, 1996.

[33] R. Larsson, P. Steinmann, and K. Runesson. Finite element embedded localization band for finite strain plasticity based on a regularized strong discontinuity. *Mechanics of Cohesive-Frictional Materials*, 4:171–194, 1998.

[34] M. Jirásek. Embedded crack models for concrete fracture. In R. de Borst, N. Bićanić, H. Mang, and G. Meschke, editors, *Computational Modelling of Concrete Structures, EURO-C98*, volume 1, pages 291–300. Elsevier, 1998.

[35] I. Stakgold. *Green's functions and boundary value problems*. Wiley, 1998.

[36] P. Steinmann, R. Larsson, and K. Runesson. On the localization properties of multiplicative hyperelasto-plastic continua with strong discontinuities. *International Journal of Solids and Structures*, 34:969–990, 1997.

[37] J. Mosler and G. Meschke. FE-modeling of displacement discontinuities in inelastic continua. *Zeitschrift für Angewandte Mathematik und Mechanik*, 81(Suppl. 4):875–876, 2001.

[38] R.I. Borja. A finite element model for strain localization analysis of strongly discontinuous fields based on standard galerkin approximation. *Computer Methods in Applied Mechanics and Engineering*, 190:1529–1549, 2000.

[39] J. Oliver. A consistent characteristic length for smeared cracking models. *International Journal for Numerical Methods in Engineering*, 28:461–474, 1989.

[40] J. Mosler and G. Meschke. Analysis of mode I failure in brittle materials using the strong discontinuity approach with higher order elements. In *2. European Congress on Computational Mechanics, CD-Rom*, 2001.

[41] J.C. Simo and S. Rifai. A class mixed assumed strain methods and the method of incompatible modes. *International Journal for Numerical Methods in Engineering*, 29:1595–1638, 1990.

[42] R. De Borst, G.N. Wells, and L.J. Sluys. Some observations on embedded discontinuity models. *Engineering Computations*, 18:241–254, 2001.

[43] J. Simo and T.J.R. Hughes. *Computational inelasticity*. Springer, New York, 1998.

[44] G. Meschke, R. Lackner, and H.A. Mang. An anisotropic elastoplastic-damage model for plain concrete. *International Journal for Numerical Methods in Engineering*, 42:703–727, 1998.

[45] J. Hofman, R. Eligehausen, and J. Ožbolt. Behaviour and design of fastenings with headed anchors at the edge under tension and shear load. In R. De Borst, J. Mazars, G. Pijaudier-Cabot, and J.G.M. Van Mier, editors, *FRActure Mechanics of COncrete Structures IV*, volume 2, pages 941–947, 2001.